SLAC/AP-113
November 1998
(AP)

Vertical Emittance Studies at the ATF Damping Ring

F. Zimmermann, K.L.F. Bane, T. Kotseroglou

Stanford Linear Accelerator Center, Stanford, CA 94309

J. Urakawa, H. Hayano, K. Kubo, T. Naito, K. Oide, N. Terunuma, N. Toge

High Energy Accelerator Research Organization (KEK), Tsukuba-shi, Ibaraki-ken, 305 Japan

T. Okugi

Tokyo Metropolitan University, Tokyo, Japan

S. Kashiwagi

The Graduate University for Advanced Studies, Ibaraki-ken, 305 Japan

Abstract

A primary purpose of the ATF Damping Ring is to demonstrate the small vertical emittance required for a future linear collider. In this report, we first describe the diagnostics available to measure this emittance. Then we discuss the dependence of the emittance on various parameters, such as the betatron tunes, vacuum pressure, and beam current, and, subsequently, study several methods of betatron-coupling correction. Next, we show that the interferometer used to determine the vertical beam size is sensitive to transverse beam tails and does not measure the core emittance, which could explain the observed sensitivity of the measured spot size to vacuum pressure and beam intensity. Finally, we summarize the results and propose a few further studies.

In the appendix, we present recent measurements of the dynamic aperture, and discuss the variation of the beta functions, *e.g.*, at the synchrotron light monitor, with the betatron tune. Here, we also present details of the SUSSIX program, by which, in the future, we hope to infer all linear coupling parameters as well as higher-order nonlinearities from turn-by-turn orbit data.

1 Introduction

The vertical emittance in the ATF Damping ring is expected to be limited by spurious vertical dispersion and by linear betatron coupling [1, 2]. Both effects would imply a strong tune dependence. For a vacuum pressure of 10 nTorr, also multiple beam-gas scattering can significantly increase the measured rms emittance. Since the vertical design emittance is extremely small, intrabeam scattering is a further prominent contribution, causing a large emittance increase at higher beam currents.

In the next section we briefly describe the diagnostics and measurement techniques which are available to measure the vertical emittance. Section 3 discusses the effect of dispersion and betatron coupling, and the search for an optimum working point in the tune diagram. This is followed, in Section 4, by a discussion of

coupling correction schemes. Section 5 points out some limitations of the interferometer measurements, and, taking these into account, investigates the importance of gas scattering and intrabeam scattering. Sections 3, 4 and 5 also describe various experimental results. In Section 6, we summarize the open questions, and suggest a series of future experiments.

Appendix A presents the results of dynamic aperture studies, in which the beam lifetime was measured for different collimation amplitudes (varied with local bumps at an aperture restriction). The amplitude where an orbit bump markedly affects the beam lifetime provides a measure of the dynamic aperture [3]. Comparing lifetime measurements on and off the difference coupling resonance allows us to distinguish the contributions from intrabeam and gas scattering. Appendix B describes the measured and simulated tune dependence of the beta functions, which is important for interpreting the interferometer spot sizes. In Appendix C, we discuss how, using the SUSSIX program [4], one can deduce amplitude and phase of all linear coupling terms as well as higher-order nonlinearities. We applied this program to simulated BPM data and present the results.

2 Diagnostics

At the ATF Damping Ring, the vertical emittance is measured using five different methods:

- synchrotron-light coherence, analyzed with a stellar interferometer ('Mitsuhashi monitor') in conjunction with simultaneous measurements of beta functions and dispersion at the radiation source point;
- wire scans in the extraction line (waist scan on single wire, or multi-wire measurement);
- Touschek lifetime;
- energy spread, determined with a profile monitor at a high-dispersion point in the extraction line;
- current-dependent bunch length, detected with a streak camera.

The last three methods exploit the fact that the Touschek effect as well as changes in the energy spread and the bunch length (the latter two assumed to be due to intra-beam scattering) depend on the vertical emittance. For tuning with the light interference pattern, the first item of our list, a simple formula of the form [5]

$$\sigma_y \approx \alpha\sqrt{\ln(1/\gamma)} \tag{1}$$

can be used to infer changes in the spot size σ_y. Here γ is the visibility of the interference pattern ($\gamma = (I_{max} - I_{min})/(I_{max} + I_{min})$ with I_{max} and I_{min} the maximum and minimum light intensity of the diffraction pattern), and α a coefficient that depends on the separation D of the double slit (*e.g.*, 40 mm), on the optical focal length f (7.04 m) and on the wavelength of the light (500 nm):

$$\alpha = \frac{\lambda f}{\sqrt{2}\pi D} \approx 20\ \mu\mathrm{m} \tag{2}$$

Results of the five different techniques should be compared carefully to uncover systematic error sources. By detecting relative changes, in principle each technique could be used for emittance optimization. The measurement of the interference pattern is the fastest and, thus, might be best suited for routine emittance tuning. Most results reported in the following were obtained with the interferometer. An important limitation of this method will be addressed later on in this report.

3 Tune Dependence: Dispersion and Coupling

At low current, three different effects determine the vertical emittance [1]: (1) residual vertical dispersion, (2) the difference coupling resonance, and (3) the sum coupling resonance. These three contributions exhibit quite a difference dependence on the betatron tunes. Measuring the vertical emittance as a function of the two tunes thus should easily distinguish between the three effects and reveal how much each one contributes to the total emittance.

3.1 Dispersion

Suppose the dispersive component of the emittance is ϵ_{y0} for a certain vertical tune ν_{y0}. It is given by an integral around the ring:

$$\epsilon_{y,d0} = \frac{\gamma^2 C_q}{\oint G^2 \, ds} \oint ds \; \mathcal{H}_y(s) \; |G(s)|^3 \tag{3}$$

with $C_q = 3.84 \times 10^{-13}$ m, $G(s)$ the inverse bending radius, and $\mathcal{H}(s)$ the dispersion invariant. As a function of the vertical tune ν_y, the dispersive emittance changes as [1]

$$\epsilon_{y,d} \approx \frac{\sin^2 \pi\nu_{y0}}{\sin^2 \pi\nu_y} \epsilon_{y,d0} \tag{4}$$

which follows from the dependence of (off-energy) closed-orbit distortions on the tune and from the fact that $\epsilon_{y,d} \sim \mathcal{H}_y$. The dispersive emittance contribution is independent of the horizontal tune. Figure 1 shows the variation of the dispersive emittance with the vertical tune, according to Eq. (4). The two curves correspond to measured or calculated emittances $\epsilon_{y,d0}$ [6] of 0.02 nm and 0.002 nm at the nominal vertical tune $\nu_{y0} = 8.72$.

3.2 Betatron Coupling

Next, consider the nearest difference coupling resonance $\nu_x - \nu_y - m \approx 0$, where m is an integer. Retaining only the slowly varying term in the Hamiltonian, the contribution to the emittance from this resonance can be estimated as [7, 8]

$$\epsilon_{y,c-} = \frac{2|\kappa_-|^2}{3|\kappa_-|^2 + \Delta\nu_-^2} \epsilon_{x0} \tag{5}$$

A similar expression describes the horizontal emittance:

$$\epsilon_{x,c-} = \frac{|\kappa_-|^2 + \Delta\nu_-^2}{3|\kappa_-|^2 + \Delta\nu_-^2} \epsilon_{x0} \tag{6}$$

Here ϵ_{x0} denotes the equilibrium horizontal emittance in the absence of coupling, $\Delta\nu_- = \nu_I - \nu_{II} - m$ is the *measured* distance to the difference resonance [1], and $|\kappa_-|$ is the driving term of the difference resonance:

$$\kappa_- = \frac{1}{2\pi} \oint K_s(s) \sqrt{\beta_x(s)\beta_y(s)} e^{i[\phi_x(s) - \phi_y(s) - (\nu_x - \nu_y - m)2\pi s/L]} \, ds \tag{7}$$

In Eq. (7), $K_s(s)$ is the strength of the skew quadrupole field at location s, and $\nu_{x,y}$ denote the horizontal or vertical tune in the absence of coupling. The measured tunes ν_I and ν_{II} are different, because the coupling

[1] Often this formula is expressed in terms of the uncoupled tunes ν_x and ν_y, in which case the coefficients are different.

of horizontal and vertical oscillations generates two new eigenmodes of oscillation. Near the difference resonance, the following relation holds [9, 10]

$$\nu_{I,II} = \frac{1}{2}\left(\nu_x + \nu_y - m \pm \sqrt{(\nu_x - \nu_y - m)^2 + |\kappa_-|^2}\right). \tag{8}$$

A similar formula with the same fractional values of $\nu_{I,II}$ describes the oscillation frequencies in the horizontal plane.

The minimum value of $|\Delta\nu_-|$ is equal to $|\kappa_-|$. For $|\Delta\nu_-| = |\kappa_-|$, the vertical emittance is half the natural horizontal emittance: $\epsilon_{y,c-} = \epsilon_{x0}/2$. Figure 2 (left) depicts the vertical emittance induced by the difference resonance, Eq. (5), as a function of $|\Delta\nu_-|$. The three curves correspond to different values $|\kappa_-|$ which were measured at various times in spring 1998 [11]. The nominal working point $|\Delta_-| = 0.45$ is far from the difference resonance. Therefore, an emittance contribution $\epsilon_{y,c-}$ of $2\%\epsilon_{x0}$ or less is expected, even for fairly large values of $|\kappa_-|$. In a previous analysis, it was found that Eq. (6) described the measured horizontal emittance well [12], giving some confidence in this approach.

The strength of the sum resonance $\nu_x + \nu_y - p \approx 0$ is measured by the equivalent driving term

$$\kappa_+ = \frac{1}{2\pi}\oint K_s(s)\sqrt{\beta_x(s)\beta_y(s)}e^{i[\phi_x(s)+\phi_y(s)-(\nu_x+\nu_y-p)2\pi s/L]}\,ds \tag{9}$$

and, using the formulae in [7, 8], an educated *guess* for the dependence of the vertical emittance on the distance to the sum resonance $\Delta\nu_+ = \nu_I + \nu_{II} - p$ is

$$\epsilon_{y,c+} \approx \frac{2|\kappa_+|^2}{5|\kappa_+|^2 + \Delta\nu_+^2}\epsilon_{x0} \tag{10}$$

and, for the horizontal emittance,

$$\epsilon_{x,c+} \approx \frac{3|\kappa_+|^2 + \Delta\nu_+^2}{5|\kappa_+|^2 + \Delta\nu_+^2}\epsilon_{x0} \tag{11}$$

Near the sum resonance, the measured and bare tunes in the vertical plane are related by

$$\nu_{I,II} = \frac{1}{2}\left(-\nu_x + \nu_y + p \pm \sqrt{(\nu_x + \nu_y - p)^2 - |\kappa_+|^2}\right). \tag{12}$$

Again, a similar formula with the same fractional values of $\nu_{I,II}$ describes the oscillation frequencies in the horizontal plane.

In this case, it is possible that $\Delta\nu_+ = 0$. The vertical emittance then equals $\epsilon_y \approx 2\epsilon_{x0}/5$. If the bare tunes ν_x and ν_y are varied beyond this point the motion becomes unstable. Figure 2 (right) shows the emittance generated by the sum resonance. With $|\Delta\nu_+| = 0.11$, the nominal working point ($\nu_x = 15.17$, $\nu_y = 8.72$) is quite close to this resonance. Therefore, we expect that $\epsilon_{y,c+}$ is the dominant emittance contribution, unless this resonance is carefully compensated or suppressed by the ring optics.

Ignoring the interference between the different effects, we may approximate the total emittance as the sum of the three contributions

$$\epsilon_y \approx \epsilon_{y,d}(|\nu_y|) + \epsilon_{y,c-}(|\Delta\nu_-|) + \epsilon_{y,c+}(|\Delta\nu_+|) \tag{13}$$

The emittances $\epsilon_{y,c\pm}$ given in Eqs. (5) and (10) are defined as $< y^2 > /\beta_y$ with β_y the beta function in the absence of coupling. These emittances are in general different from the eigenmode emittances. In addition, by only accounting for the slowly oscillating terms in the Hamiltonian, Eqs. (5) and (10) do not necessarily describe the local beam size correctly, and $< y^2 > /\beta_y$ may not be a well defined quantity [13].

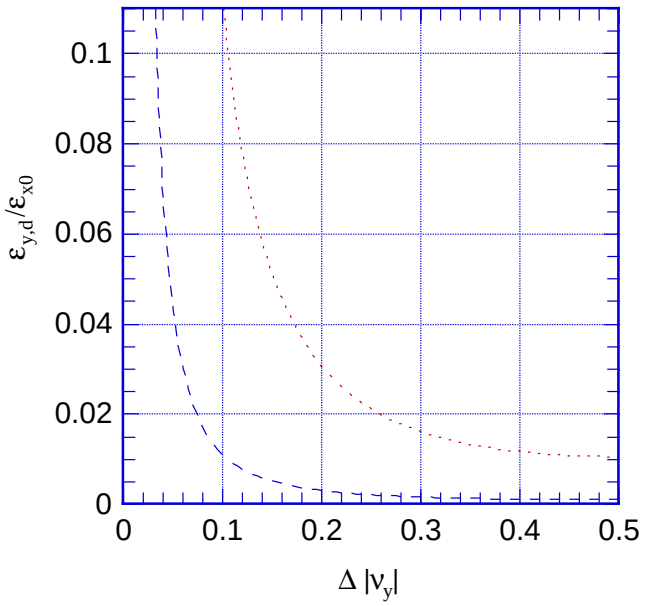

Figure 1: Vertical emittance due to dispersion, $\epsilon_{y,d}$, predicted by Eq. (4), in units of ϵ_{x0}, as a function of the fractional vertical tune $k - \nu_y$ ($k = 9$ for the ATF). The two curves correspond to $\epsilon_{y0} = 0.02$ nm and $\epsilon_{y0} = 0.002$ nm at $\nu_{y0} = 8.72$.

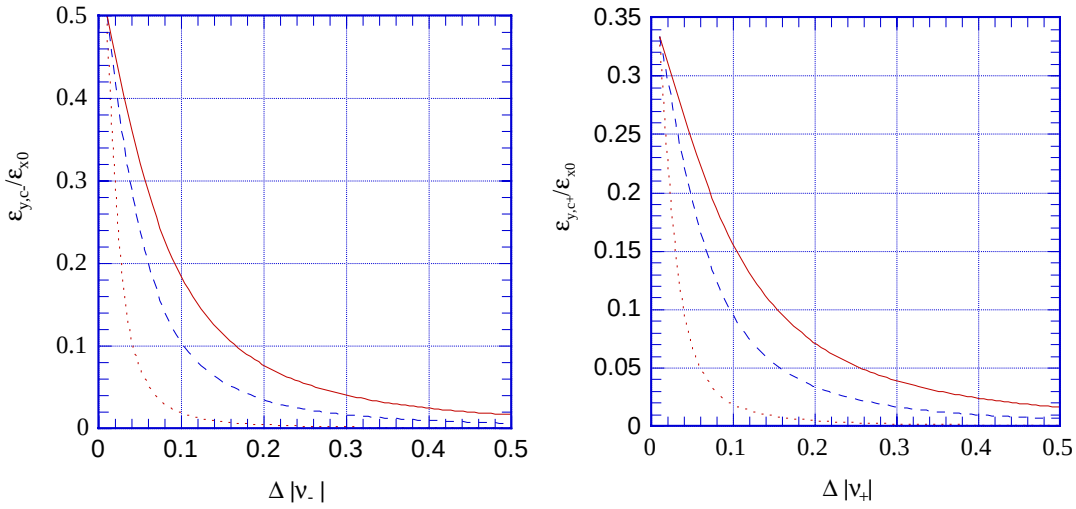

Figure 2: Vertical emittance due to the difference (left) and sum coupling resonance (right), $\epsilon_{y,c+}$ and $\epsilon_{y,c+}$, as predicted by Eqs. (5) and (10). The vertical emittance is plotted in units of ϵ_{x0}, as a function of the distance to the resonances, $\Delta\nu_-$ and $\Delta\nu_+$. The three curves correspond to three different values of the driving terms $|\kappa_-|$ and $|\kappa_+|$ (0.01, 0.03 and 0.05).

Using a different approach, based on a perturbation expansion, far from the linear coupling resonances the vertical emittance contribution due to weak betatron coupling may also be written as [1]

$$\gamma\epsilon_{y,c} = \frac{C_q\gamma^3}{16\oint G^2 ds}\ \oint \mathcal{H}_x|G^3|\left[\sum_{\pm}\frac{|W_{\pm}(s)|^2}{\sin^2\pi(\Delta\nu_{\pm})} + 2\mathrm{Re}\frac{W_{+}^{*}(s)W_{-}(s)}{\sin\pi(\Delta\nu_{+})\sin\pi(\Delta\nu_{-})}\right]ds \tag{14}$$

where $C_q = 3.84\times10^{-13}$ m, $\mathcal{H}_x$ denotes the horizontal dispersion invariant, and $G = 1/\rho$ the inverse bending radius; $*$ is the complex conjugate, Re gives the real portion of its argument, $\Delta\nu_{\pm} = nu_x \pm \nu_y - n$, the sum is over all integers n, and the functions $W_{\pm}(s)$ are

$$W_{\pm}(s) = \int_s^{s+L} dz\ K(z)\sqrt{\beta_x\beta_y}e^{i[(\phi_x(s)\pm\phi_y(s))-(\phi_x(z)\pm\phi_y(z))+\pi(\nu_x\pm\nu_y)]}. \tag{15}$$

Also in this approach, the total emittance may be approximated as the sum of the components

$$\epsilon_y \approx \epsilon_{y,d}(|\nu_y|) + \epsilon_{y,c}(\Delta\nu_-, \Delta\nu_+) \tag{16}$$

By including all Fourier harmonics n, Eq. (14) is more accurate than Eqs. (5) and (10). However, because it is a perturbation expansion, this equation is not valid close to the coupling resonances. There does not appear to be a trivial relationship between the resonance driving terms $\kappa_{\pm}$ and the functions $W_{\pm}(s)$.

3.3 Emittance Calculations with MAD

We have performed a simulation with MAD [14], which calculates the emittances using 6×6 one-turn transport matrices following a recipe developed by Chao [15]. In the simulation, the main focusing quadrupoles QF2R were randomly misaligned vertically, with a Gaussian distribution of 200 μm rms. These misalignments resulted in the spurious vertical dispersion of Fig. 3.

The expected tune dependence of the vertical emittance was explored by varying the strength of the QF2R quadrupoles. The results are illustrated in Fig. 4. A strong blow up is visible near the difference resonance, on which superimposed is a gradual increase as the vertical tune approaches the integer resonance. There is no evidence for a dependence on the distance to the sum resonance. This is surprising, since it is in apparent contradiction to Eqs. (10) or Eq. (14). In agreement with our expectation, also no dependence on the horizontal tune is seen.

How does the MAD calculation of the emittance (the smaller eigenmode emittance) based on the 1-turn transfer matrix compare with our analytical estimates in Eqs. (13) and (16)? To answer this question, we calculated the coupling driving terms $\kappa_{\pm}$ of Eqs. (7) and (9), the functions $W_{\pm}(s)$ of Eq. (15), and the dispersive emittance of Eq. (3), for the same twiss parameters and closed orbit distortion as in the MAD simulation. At a certain working point with fractional tunes[2] $\nu_x = 0.8238$ and $\nu_y = 0.3123$, we found $|\kappa_+| \approx 0.01$, $|\kappa_-| \approx 0.03$, $\epsilon_{y0} \approx 12.5$ pm, and then extrapolated from here to other tunes, using Eqs. (4), (10) and (5). Figure 5 (left) compares this simple estimate with the smallest eigenmode emittance calculated by MAD [15]. The behavior near the difference resonance is described fairly well by the analytical expression, but the MAD calculation does not show the expected emittance increase near the sum resonance. We tentatively ascribe this to the fact that the MAD/Chao algorithm ignores the off-diagonal elements in the diffusion matrix, which can become important near linear resonances [16, 17]. Calculations with SAD [18], which uses the formalism of Ref. [17], indeed do show a blow-up on the sum resonance [19]. The right picture in Fig. 5 compares the MAD simulation with an estimate based on the alternative expressions of Eqs. (4), (14) and (16), also extrapolated from the same working point. The result is quite similar, although, for most tune values, the difference to the MAD calculation is larger.

[2] From now on the symbol ν designates the fractional tune, ignoring the integer part.

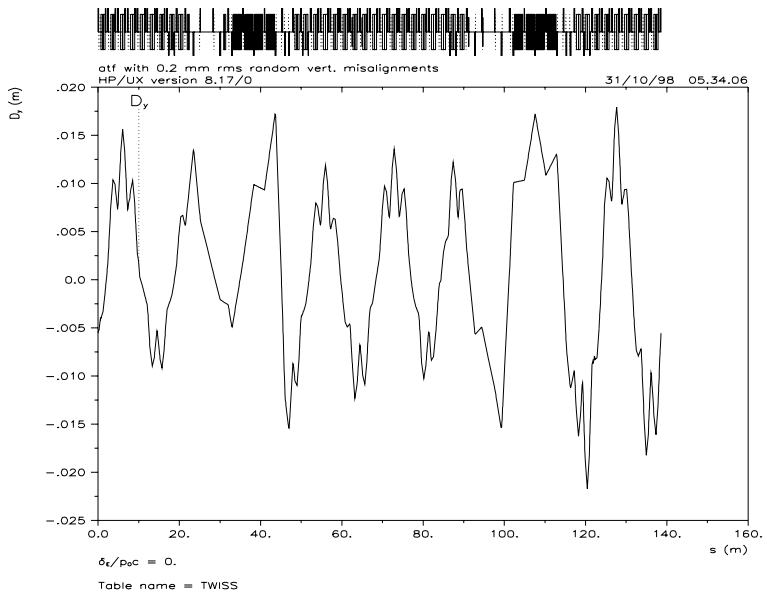

Figure 3: Spurious vertical dispersion for 200 μm rms random vertical misalignments of the QF2R quadrupoles, according to a simulation with MAD.

3.4 Measured Tune Dependence

As discussed above, the emittance should change as a function of the betatron tunes. A first experimental test, near the (calculated) working point $\nu_x = 15.55$ and $\nu_y = 8.62$ indicated a strong tune dependence. This initial result is depicted in Fig. 6. A change in visibility from 0.7 to 0.25, seen in the left picture, corresponds to a variation in spot size between 27 and 46 μm (almost a factor 4 change in emittance!). Since, at the time of this measurement the tune monitor was not available, we *calculated* the tune variation induced by the changes in quadrupole strength. The emittance inferred from the visibility is shown in the right picture, plotted as a function of the calculated distance to the sum resonance. Also depicted is the result of a nonlinear 3-parameter fit to Eq. (10) with an additional constant term, ϵ_{y0}. The fit result is $|\kappa_+| \approx 5 \times 10^{-4}$, $\epsilon_{y0} \approx 50$ pm (or 5% of the horizontal emittance), and a value for the offset in the sum of the two unknown tunes, $\Delta(\nu_I + \nu_{II})$. This measurement must be taken with great care, however, because the intensity of the stored beam was different for different tune values, and, as we shall see later, the beam intensity can strongly affect the measured spot size.

Figures 7 (a)–(c) show the result of a more detailed study, which was performed two days later, around the nominal working point with measured fractional tunes of 0.16 and 0.72. During this measurement the beam current was more stable. Depicted in Fig. 7 is the observed dependence of the beam size on the vertical tune, and on the distance to the two coupling resonances. In this case, somewhat unexpectedly, the measured emittance assumed a minimum value close to the sum resonance. No data were taken on the sum resonance itself, since beam could not be stored here, either because of this very resonance or because the vertical tune crossed the third integer resonance near this point.

From the observed weak tune dependence we conclude that, at the nominal working point, the spot size measured with the interferometer is limited neither by dispersion nor by betatron coupling. A possible

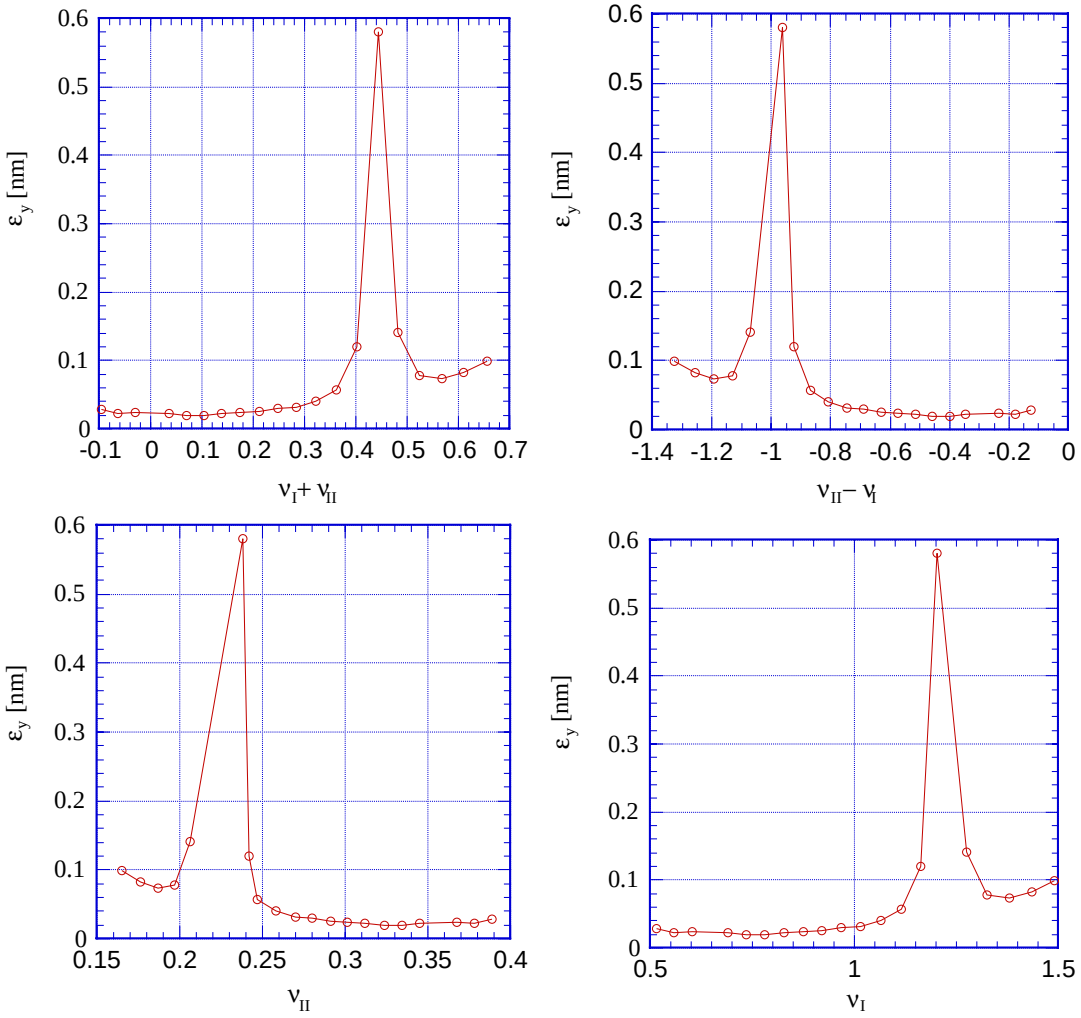

Figure 4: Simulated vertical emittance as a function of $(\nu_I + \nu_{II})$, $-(\nu_I - \nu_{II})$, ν_{II} and ν_I, respectively. The fractional tunes ν_I and ν_{II} were varied by changing the strength of the main quadrupole family. The peak is due to the difference resonance, the gradual variation due to dispersion. A contribution from the sum resonance is not visible.

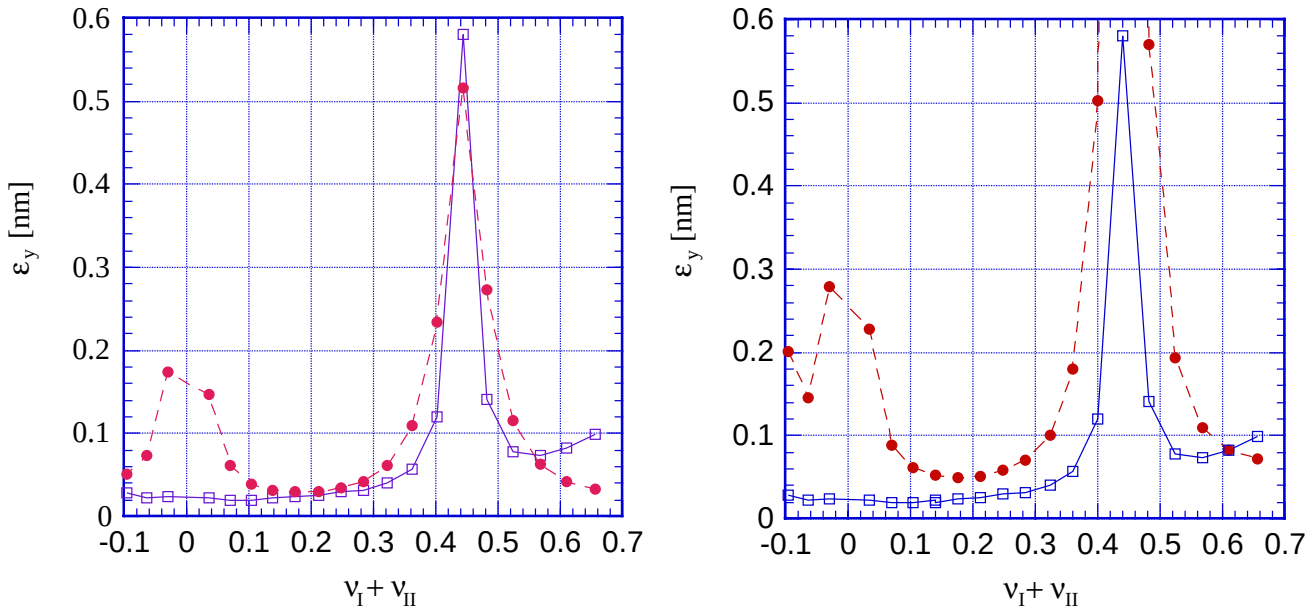

Figure 5: Emittance simulated by MAD [14] using the Chao formalism [15] (solid line, squares) and the simpler estimates based on Eqs. (13), (5), (10) and (4) (left figure dashed line and circles) and on Eqs. (13), (14) and (4) (right figure dashed line and circles) as a function of the distance to the sum resonance, for 200 μm rms vertical quadruple displacements. The coupling driving terms $\kappa_{\pm}$ and the dispersive baseline emittance ϵ_{y0} as well as the functions $W_{\pm}(s)$ were evaluated at the fractional tunes $\nu_I + \nu_{II} = 0.136$ and $\nu_{II} = 0.312$.

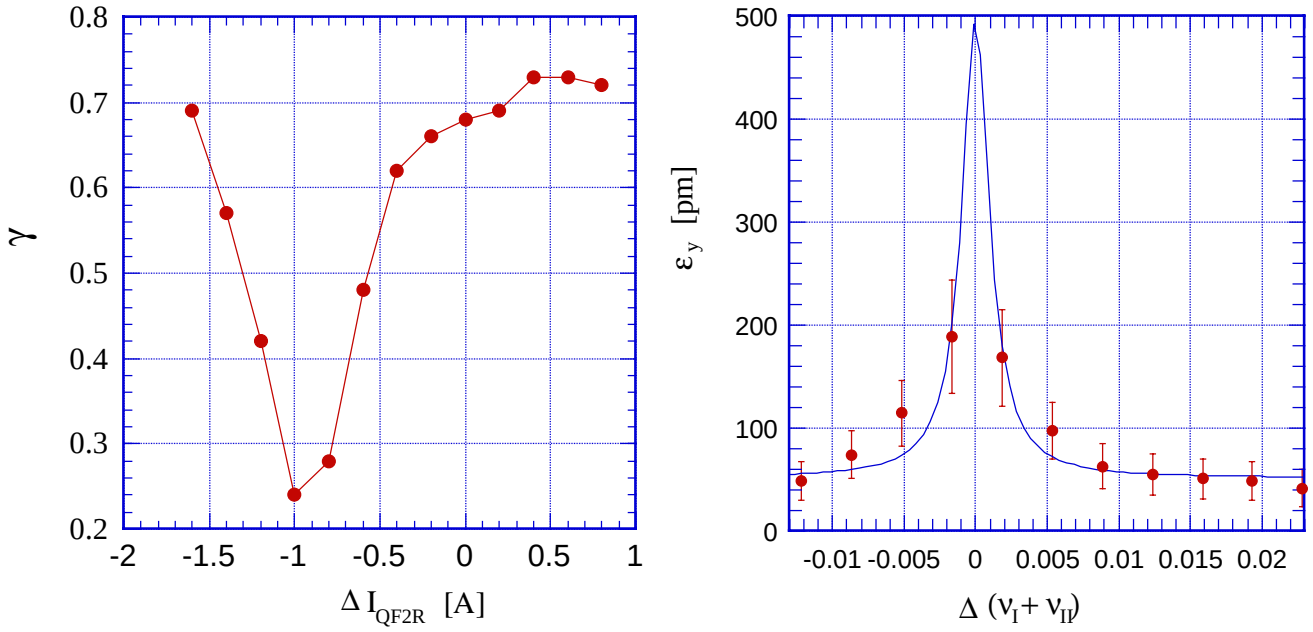

Figure 6: Left: measured visibility of SR monitor vs. the change in strength of the main quadrupole string QF2R. A change by 1 A corresponds to a horizontal tune change of about 0.04. The range of visibility values covers spot sizes between 27 μm (for $\gamma = 0.7$) and 46 μm ($\gamma = 0.25$). Right: inferred vertical emittance vs. the estimated change in the distance to the sum resonance, and the result of a nonlinear fit to Eq. (10) with an additional constant term ϵ_{y0}. The fitted parameters are $|\kappa_+| \approx 5 \times 10^{-4}$ and $\epsilon_{y0} \approx 50$ pm, plus a value for the horizontal offset. The error bars shown correspond to an assumed uncertainty in the visibility measurement of about 10%. This is probably a large overestimate of the actual error.

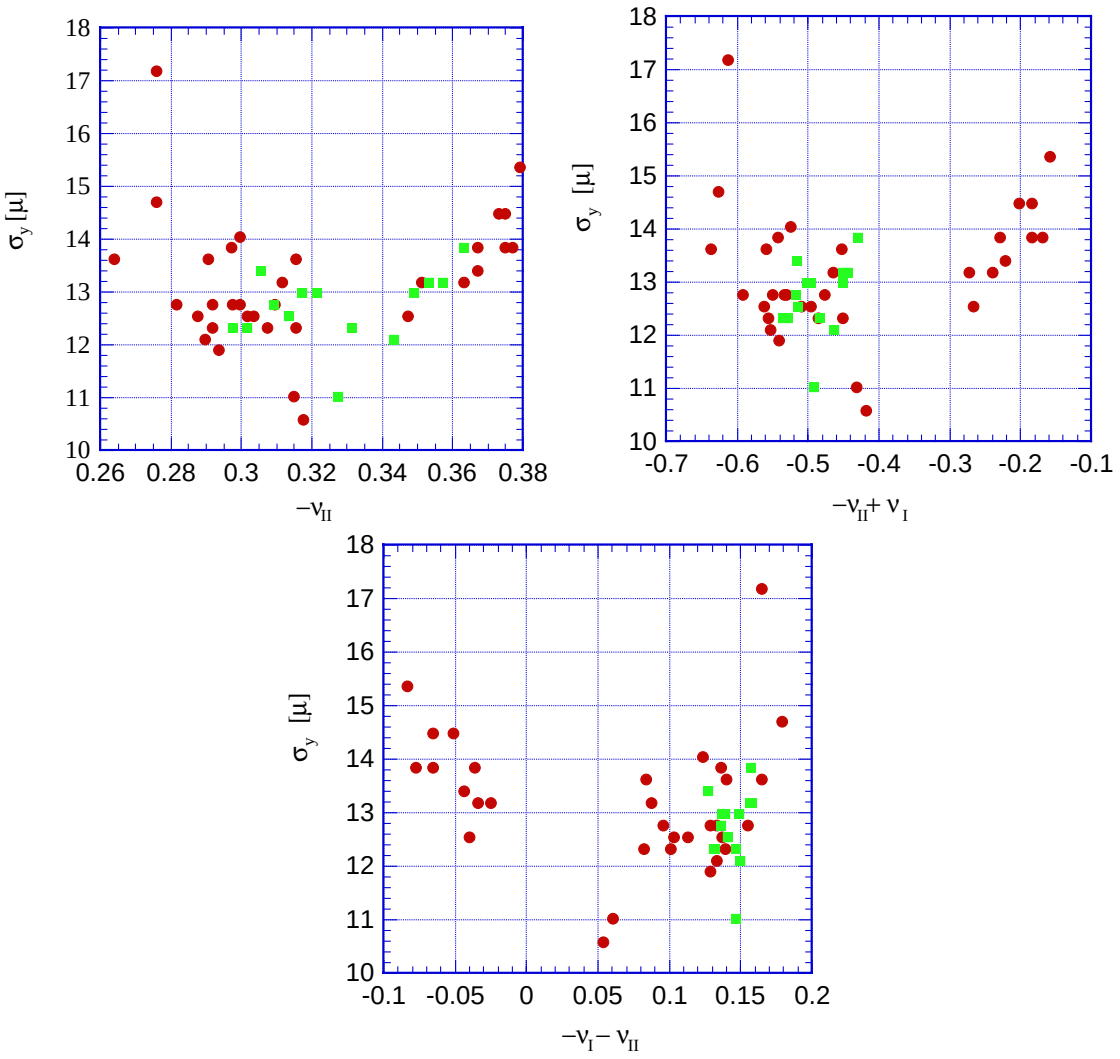

Figure 7: Measured vertical beam size, inferred from the SR interferometer, plotted as a function of (a) the vertical tune, (b) the distance to the difference resonance, (c) the distance to the sum resonance. The tunes were varied by changing the strength of the quadrupole strings QF2R (circles) and QF1R (squares).

explanation is discussed in Section 5.

4 Coupling Correction

4.1 Sextupole Orbit Bumps

For orthogonal correction of dispersion and coupling we can use double orbit bumps separated by appropriate phase advances, as illustrated in Fig. 8. Similar orthogonal bumps are used for sextupole alignment at the SLC final focus [20]. The scheme makes use of the fact that the nominal phase advance per cell is 132.8° horizontally and 45.6° vertically. Therefore, the R matrix over 4 cells is a nearly perfect $-I$ transform in both planes. The two dispersion bumps are shifted with respect to each other by 90° in the vertical plane, or by 2 arc cells, so that they control the two phases of the dispersion function.

The sine and cosine like terms of the difference coupling resonance can be corrected by two symmetric bumps, shifted by only one cell, for which $\Delta(\phi_x - \phi_y) = -\pi/2$. Unfortunately, because over one cell the sum of the two betatron phases changes by π, $\Delta(\phi_x + \phi_y) = -\pi$, it is difficult to control the second phase of the sum resonance. In addition, a bump can control only one of the two resonances [3]. The nearest resonance will be dominant, and it is primarily this resonance which must be compensated.

We can estimate the magnitude of the orbit bumps as follows. The coupling term introduced by a symmetric vertical double bump of amplitude Δy is approximately

$$\Delta|\kappa_+| \approx \frac{1}{2\pi} 4\ (\Delta y)\ K_{sext}\sqrt{\beta_x \beta_y} \tag{17}$$

where K_{sext} is the integrated strength of the main sextupole, and $\beta_{x,y}$ is the beta function at the sextupole. A factor of 2 accounts for the double bump. Solving for Δy we find

$$\Delta y \approx \frac{\pi|\kappa_+|}{\sqrt{\beta_x \beta_y} K_{sext}} \tag{18}$$

For example, if the vertical emittance is 10% of the horizontal, and entirely due to the sum resonance, $|\kappa_+| \approx 0.04$, according to Fig. 2. With $K_{sext} \approx 50$ m^{-2} and $\beta_{x,y} \approx 3$ m, the required offset is $\Delta y \approx 0.3$ mm. In reality there is a partial cancellation, by about a factor 2–3, between the effects of orbit offsets in the focusing and defocusing sextupoles, so that the real bump amplitude would be about 1 mm.

Simulations with the MAD program [14] indicate, however, that a vertical 4-corrector bump with 1-mm amplitude at a focusing sextupole increases the emittance of the second (quasi-vertical) eigenmode by only about 0.2%. This is illustrated in Fig. 9, which also demonstrates that at some working points the emittance is affected by the difference resonance and at others by the sum resonance. According to the figure, local 1-mm orbit bumps at the sextupoles will not have a large effect on the eigenmode emittance. The weak dependence is in apparent contradiction to Eqs. (10) and (17), but it is, of course, consistent with the MAD calculation results reported earlier.

In Fig. 10 we depict *measurements* of the effect of local orbit bumps on the beam size. The measured dependence is rather small, as predicted by MAD, and, furthermore, the optimum bump amplitude is usually close to the nominal value (zero).

[3] It is possible that a bump corrects both resonances at the same time, given that most or all of the coupling is generated by the sextupoles, which for the present betatron tunes are all located at roughly the same phase.

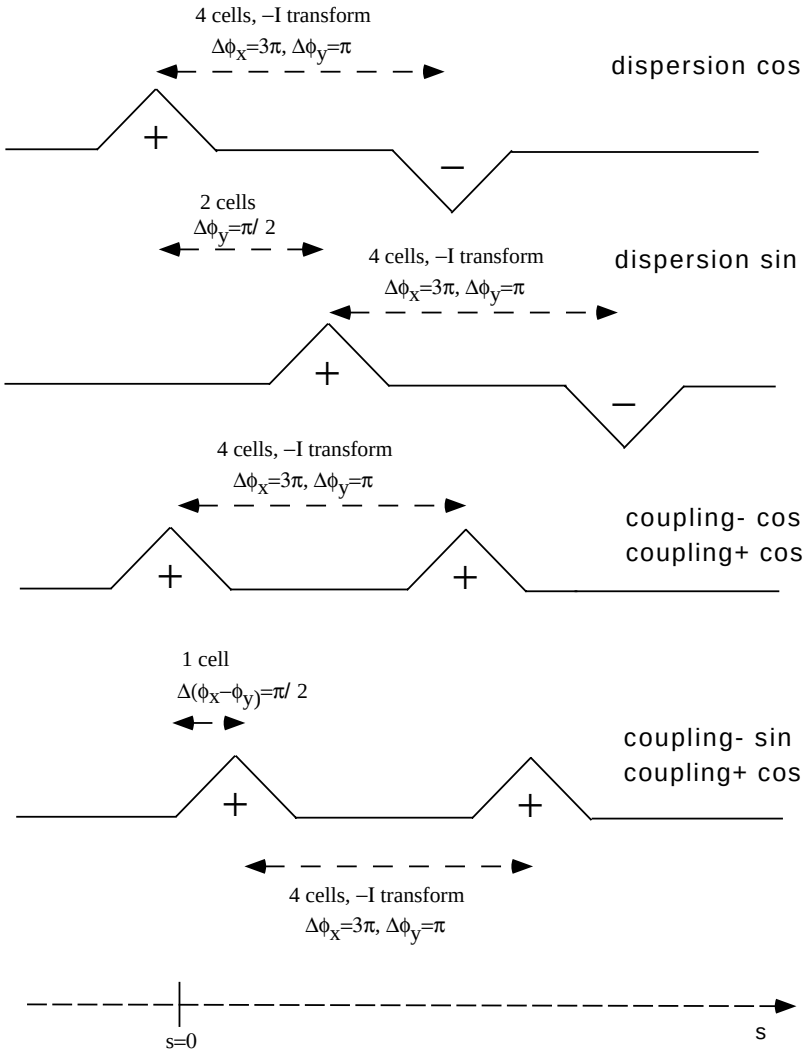

Figure 8: Vertical bumps for orthogonal coupling and dispersion control. The symbols + and − represent the sum and difference resonance, respectively.

4.2 Skew Quadrupoles

In addition to vertical orbit bumps in sextupole magnets, the coupling can also be controlled via 4 skew quadrupole coils. These are sextupole trim coils wired as skew quadrupoles [21]. The main sextupole coil, consisting of 12 turns, carries a maximum current of 325 A, which corresponds to a sextupole gradient $\partial^2 B_z/\partial x^2$ of 6000 Tm^{-2}. The trim coil has 20 turns per pole with a maximum current of 10 A. The sextupole length l_{sext} is 6 cm, and the pole-tip radius is $a = 16$ mm. The integrated maximum strength of a skew quadrupole can be estimated as

$$K_{skew,\max} \approx \frac{1}{2}\frac{\partial^2 B_z}{\partial x^2}\frac{l_{sext}a}{B\rho} \approx 0.03 \text{ m}^{-1} \tag{19}$$

which is marginally sufficient to correct a coupling coefficient of $|\kappa_{\pm}| \approx 0.03$, and roughly equivalent to the effect of a 1-mm vertical orbit bump across one pair of SF/SD sextupoles. Table 1 lists the 4 available skew quadrupoles and the betatron phases at their locations [22]; the betatron phases for the first skew quadrupole were set to zero [4]. Table 1 shows that there is no $-I$ pair of skew quadrupoles (a $-I$ pair would correspond to a phase advance of 180° or 540°). This possibly complicates the orthogonal tuning with these magnets.

skew quadr. name	ϕ_x	ϕ_y
SD15	0°	0°
SD16	45°	135°
SD21	270°	810°
SD22	315°	945°

Table 1: Approximate betatron phases at the skew quadrupole magnets.

Figure 11 presents a typical measurement result, showing only a small effect of the skew quadrupole setting on the measured beam size. This is not incosistent with the MAD calculation depicted in Fig. 12, where for the maximum excitation of a single skew quadrupole the emittance changes by a meager 6 pm, or 0.6% of the horizontal emittance.

4.3 Coupling Strength from Transverse Oscillations

Turn-by-turn orbit data taken at two BPMs will allow us to determine all four coupling terms and the appropriate correction procedure from the amplitude and phase of the lowest-order resonance lines in the frequency spectrum. This analysis can be performed easily using the SUSSIX program [23, 4]. The formalism and the program usage are explained in Appendix C.

[4] The beta functions at the skew quadrupoles are about $\beta_x \approx 1.9$ m and $\beta_y \approx 3.5$ m.

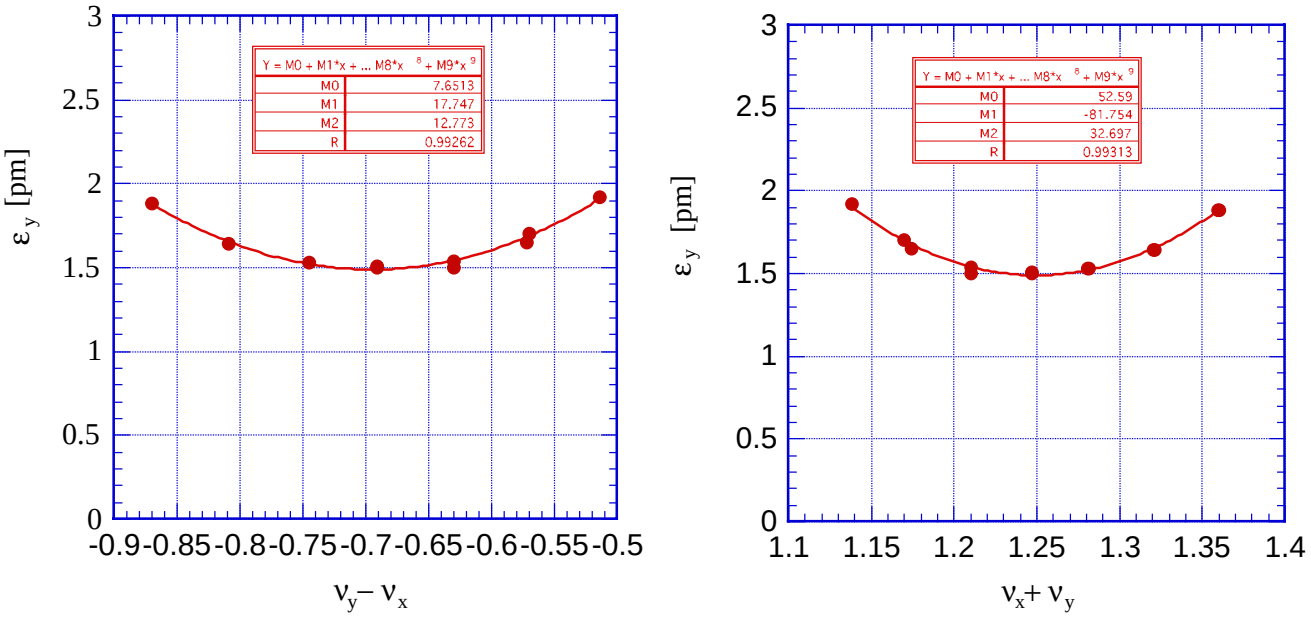

Figure 9: Simulated emittance of the smaller transverse eigenmode as a function of distance from the sum resonance (top) and from the difference resonance (bottom). For each working point a vertical bump of 1 mm amplitude was generated across 1 pair of focusing and defocusing sextupoles.

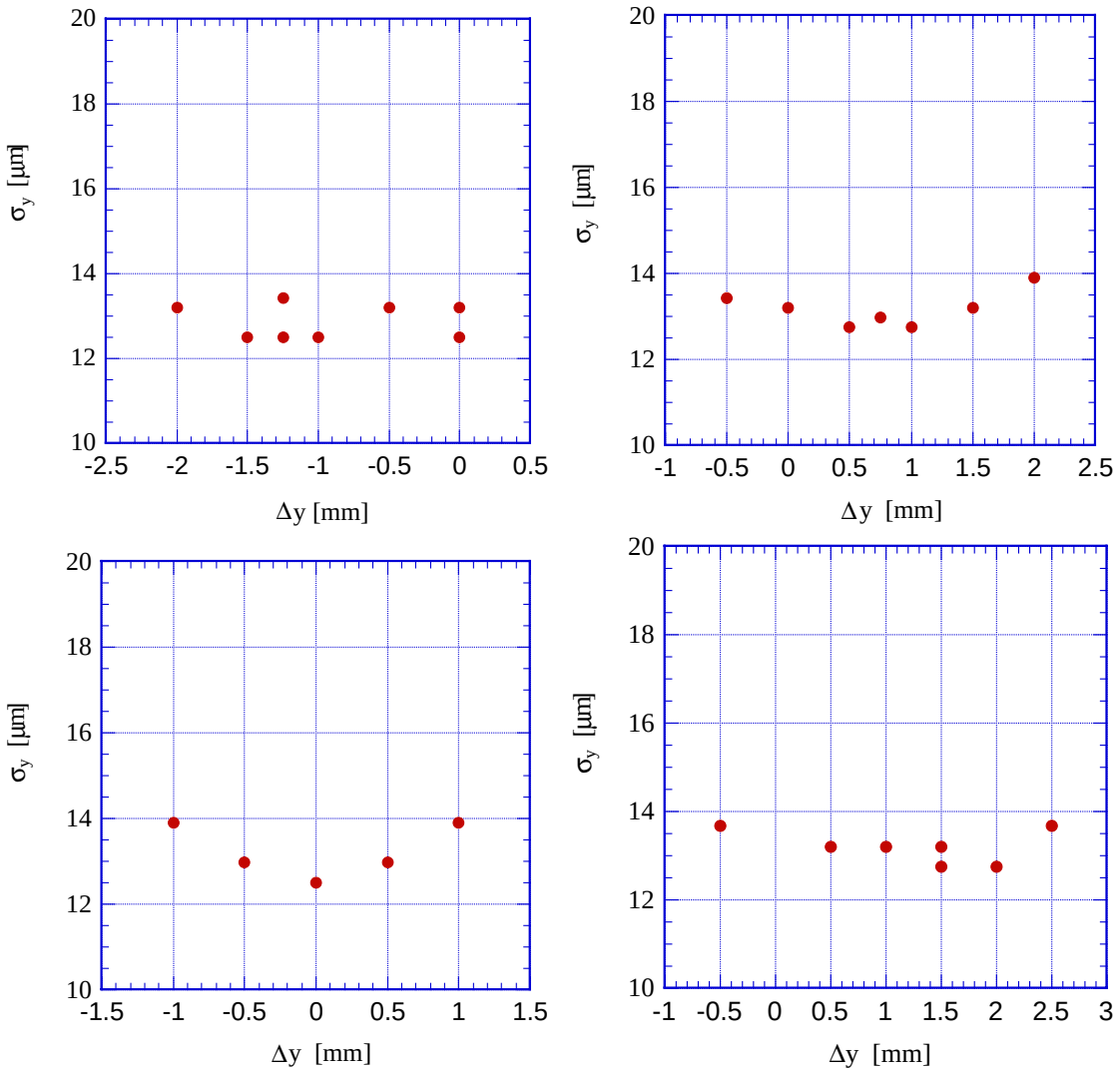

Figure 10: Vertical beam size inferred from the SR interferometer as a function of local-bump amplitude at various beam-position monitors: BPM 2 (top left), 6 (top right), 10 (bottom left) and 14 (bottom right).

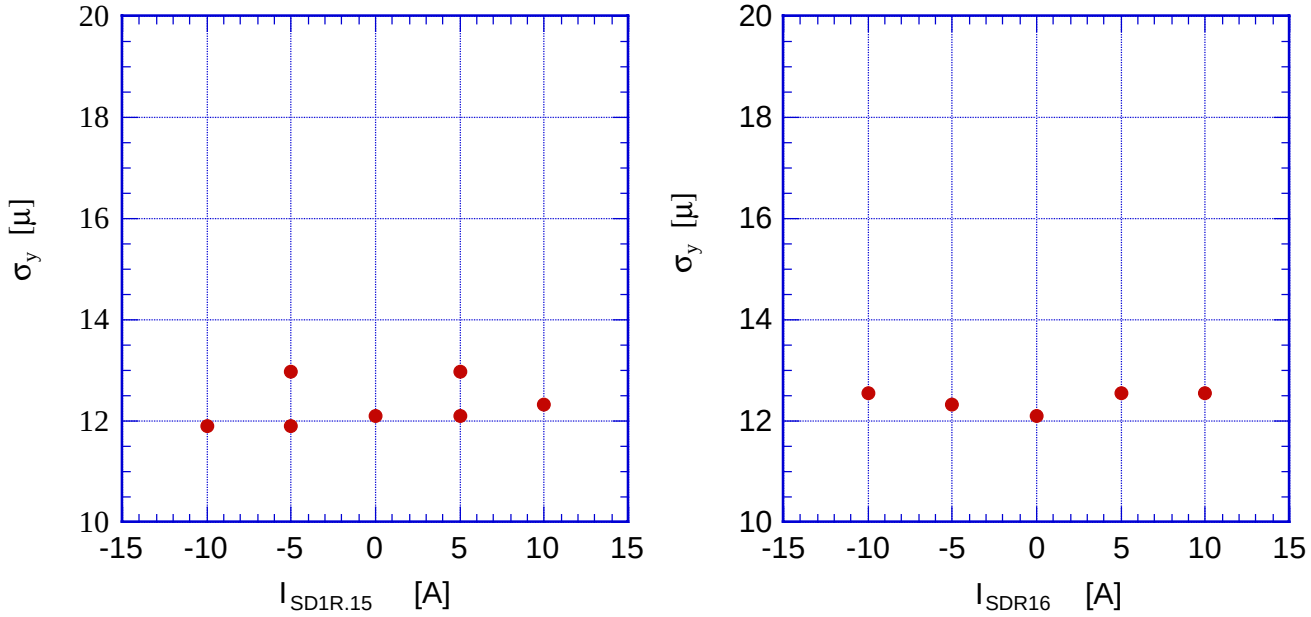

Figure 11: Vertical beam size inferred from the SR interferometer as a function of excitation of two different skew quadrupole magnets.

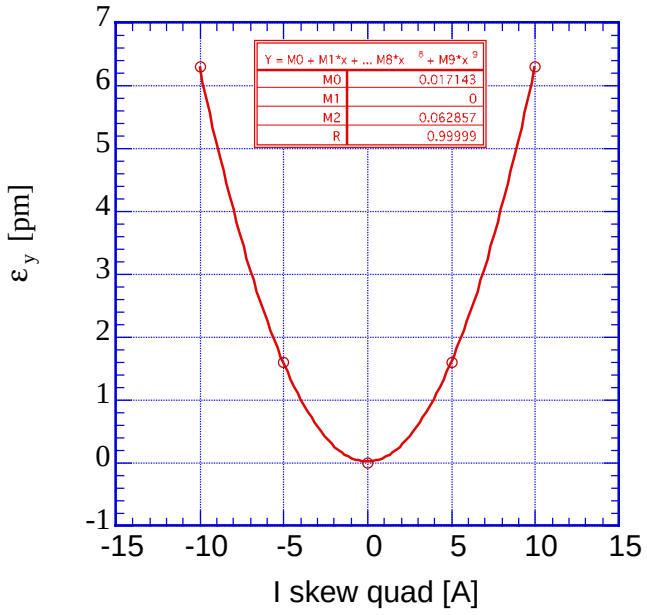

Figure 12: Simulated vertical emittance as a function of the skew quadrupole strength SD1R.15 in units of A.

5 Intensity Dependence: Gas Scattering and Intrabeam Scattering

Figure 13 shows that the vertical beam size measured with the interferometer depends strongly on the bunch current. To infer the spot size from the spatical coherence the van Cittert Zernike theorem is invoked. There

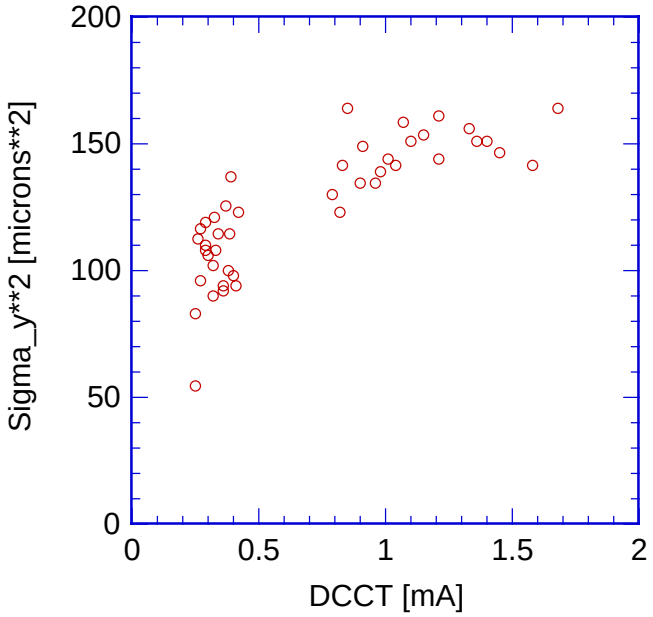

Figure 13: Measured variation of the square of the beam size with the stored beam current.

are some uncertainties whether this theorem can be applied to the vertical spot size [24, 25]. These are related to the wavelength dependence of the photon angular divergence, the non-Gaussian character of the photon distribution, and to the change in coherence induced by the antechamber aperture [24, 25]. For now we assume the theorem is applicable, and ask what exactly do we measure then?

The interferometer measures the coherence, or visibility, of the synchrotron radiation, which is proportional to an integral of the form

$$\gamma \propto \int e^{i\alpha y} I(y)\, dy \approx 1 - \frac{\alpha^2}{2} < y^2 > + \mathcal{O}(\alpha^4 < y^4 >) \tag{20}$$

where $I(y)$ is the vertical intensity distribution of the light source (the beam), and $\alpha = kD/L$, with D the distance between the slits, k the wave number, and L the distance between the light source and the plane where the coherence is estimated. Equation (20) shows that the interferometer signal is approximately determined by the rms of the beam distribution. It does not provide a measure of the core emittance, that is of primary interest for linear-collider applications. By retaining also higher order terms in the above expansion, we see that transverse tails are weighted even more strongly than in an rms sense.

Two processes generating transverse tails which depend on the beam intensity are scattering on the residual gas and intrabeam scattering. The former is intensity dependent since the vacuum pressure of the ring changes with the beam current; the latter since the collision rate increases with the beam density.

From previous analyses of the ATF beam lifetime [6, 26] we expect that for present operating conditions residual-gas scattering is the dominant effect.

5.1 Gas Scattering

The rms emittance growth due to multiple gas scattering can be estimated from

$$\epsilon_y = \epsilon_{y0} + < \beta_y > \tau_y \frac{\Delta < \theta^2 >}{\Delta t} \tag{21}$$

where ϵ_{y0} is the emittance generated by synchrotron radiation for an ideal zero pressure, τ_y is the vertical damping time (about 20 ms), $< \beta_y >$ the average vertical beta function (3.5 m), and [27]

$$\frac{\Delta < \theta^2 >}{\Delta t} \approx \left(\frac{14.1 \text{ MeV}}{pc} \right)^2 \frac{\rho c}{X_0} \tag{22}$$

with X_0 the radiation length and ρ the mass density of the gas molecules. A typical radiation length is $X_0 \approx 40$ g/cm^2. At a CO pressure of 30 nTorr, the rms emittance due to multiple gas scattering then would be 0.28 nm. Equation (22) describes the effect of multiple scattering accurately to within a few percent for times [27] $t > 10^{-3} X_0/(c\rho)$, which for our numerical example amounts to $t > 30$ ms. The expected emittance due to residual gas scattering, according to Eqs. (21) and (22), is depicted as a function of the carbon-monoxide pressure in Fig. 14.

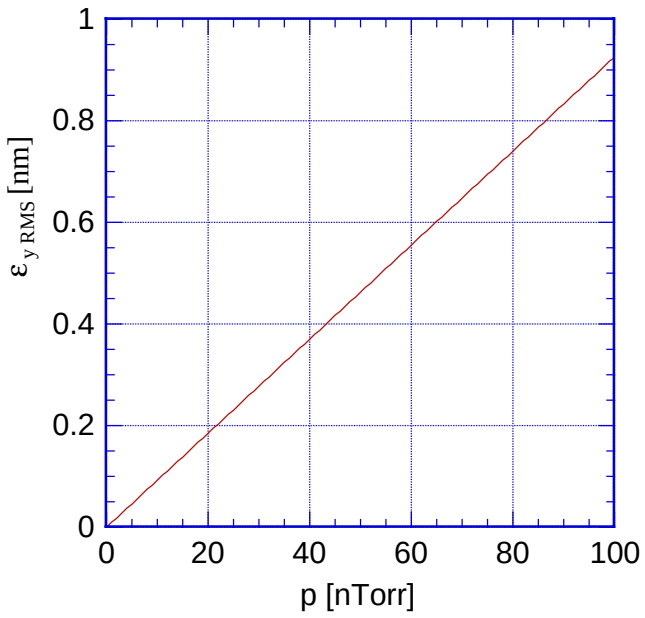

Figure 14: Predicted vertical rms emittance due to multiple residual-gas scattering as a function of the average gas pressure, according to Eq. (21).

Figure 15 shows the measured pressure dependence of the vertical emittance, as deduced from the interferometer spot size. The slope is roughly consistent with the expectation, and extrapolation to zero pressure indicates an emittance of 11 pm (or 1% coupling). This is equal to the ATF design goal.

5.2 Intrabeam Scattering

Intrabeam scattering in electron and proton storage rings has been analyzed by various authors [28, 29, 30]. The current-dependent emittance contribution from intrabeam scattering can be calculated, for example,

using the formulae of Ref. [28]. Assuming that the energy spread induced by intrabeam scattering contributes to the emittance in the same way as the energy spread arising from synchrotron radiation, the total emittance is simply

$$\epsilon_y \approx \epsilon_{y0} \left(1 + \left(\frac{\sigma_{\delta,\mathrm{IBS}}}{\sigma_{\delta 0}} \right)^2 \right) \tag{23}$$

where ϵ_{y0} denotes the zero-current emittance, $\sigma_{\delta 0}$ the rms energy spread due to synchrotron radiation and $\sigma_{\delta,\mathrm{IBS}}$ the additional rms energy spread induced by intrabeam scattering, to be added in quadrature. The energy spread due to intrabeam scattering is given as the solution of a cubic equation [28]

$$\sigma_{\delta,\mathrm{IBS}}^2 \left(1 + \sigma_{\delta,\mathrm{IBS}}^2 \right)^2 \approx \left\langle \frac{N_b r_e^2 c \beta_x \tau_\delta}{2^5 \pi \gamma^3 \sigma_{x0}^2 \sigma_{y0} \sigma_{z0}} f(\chi_m) \right\rangle \tag{24}$$

where r_e is the classical electron radius, the σ's with subindex 0 refer to the rms beam size at zero current, the angular brackets represent an average around the ring, and $f(\chi_m)$ is a slowly varying function of $\chi_m = r_e \beta_x^2 / (b_{max} \gamma^2 \sigma_x^2)$ [28], where $b_{max} = (N_b / ((2\pi)^{3/2} \sigma_x \sigma_y \sigma_z))^{-1/3}$. We consider $f(\chi_m)$ as roughly constant (equal to 250), and independent of the beam current.

Figure 16 shows the calculated variation of the vertical emittance with beam current for four different zero-current emittance coupling ratios. In this calculation, an rms energy spread of $\sigma_{\delta 0} \approx 7.2 \times 10^{-4}$, a longitudinal damping time of $\tau_\delta \approx 20$ ms, and a horizontal emittance of 1.1 nm were assumed. Simulations with MAD using the Bjorken-Mtingwa formalism [30] give similar results.

In principle, the above formulae overestimate the actual growth of the core emittance [31], because for large momentum exchanges the intrabeam scattering rate can be comparable to the damping time. This would result in tails of the form $\sim 1/y^3$, due to rare single scattering, but would not affect the core of the beam. In order to estimate the real core emittance, the integration over the (normalized) transverse momentum distribution should be cut off at a (normalized) momentum change [31]

$$q^* \approx \left(\frac{\tau_e r_e^2 c N_b}{3 \gamma^3 \sigma_x \sigma_y \sigma_z \sigma_{x'}} \right)^{1/2} . \tag{25}$$

This can be included in the formulae of Ref. [28] by replacing the integral

$$f(\chi_m) = \int_{\chi_m}^{\infty} \frac{1}{\chi_m} \ln \left(\frac{\chi}{\chi_m} \right) \, e^{-\chi} \, d\chi \tag{26}$$

with

$$\bar{f}(\chi_m) = \int_{\chi_m}^{\chi^*} \frac{1}{\chi_m} \ln \left(\frac{\chi}{\chi_m} \right) \, e^{-\chi} \, d\chi \tag{27}$$

where $\chi^* \approx (q^* / \gamma \sigma_{x'}^2)^2$. Inserting the approximate average values $\sigma_x \approx 95$ μm, $\sigma_y \approx 6.2$ μm, and $N_b \approx 10^{10}$, we find $\chi_m \approx 4 \times 10^{-6}$, and $\chi^* \approx 6 \times 10^4$. Because $\chi^* \gg 1 \gg \chi_m$ and due to the exponential term $e^{-\chi}$ in the integrand of Eq. (27), the calculated emittance increase is the same with and without the additional cutoff χ^* [5]

As we have discussed above, the interferometer measures the rms emittance (or larger) including any tails that may be present. This feature can be taken advantage of. Figure 16 indicates that, if the tails are primarily due to intrabeam scattering, maximizing the dependence of the beam size on the beam current would be one promising approach to optimize the vertical emittance.

[5] This is inconsistent with earlier results [31]; so maybe there is a flaw in our derivation.

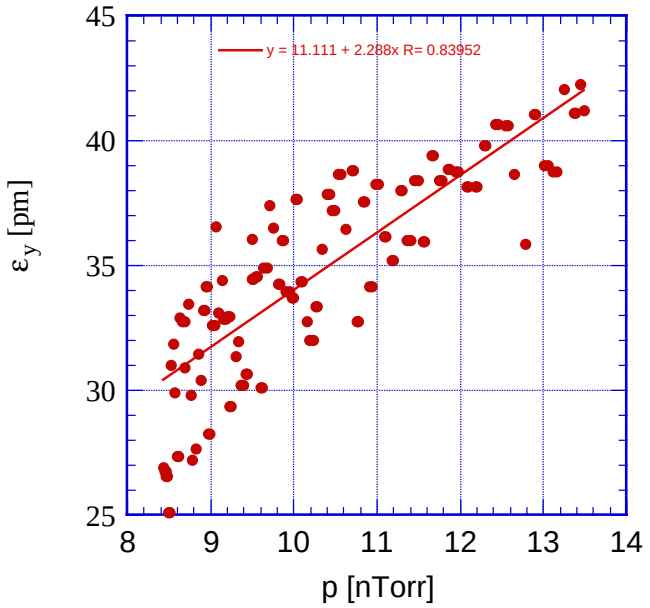

Figure 15: Measured vertical emittance inferred from the interferometer spot size as a function of gas pressure.

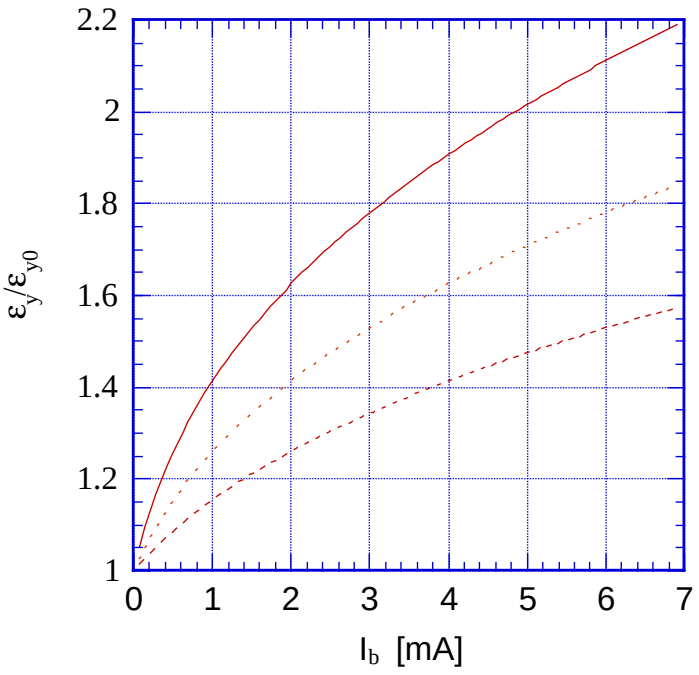

Figure 16: Relative increase of the vertical emittance, ϵ_y/ϵ_{y0}, due to intrabeam scattering as a function of the beam current in mA, for four different values of emittance coupling, calculated using the formulae of Ref. [28].

If intrabeam scattering is a significant source of energy spread and emittance, a reduction of the rf voltage should decrease the emittance. Unfortunately, interferometric spot-size measurements for different rf voltages at $N_b \approx 5 \times 10^9$ gave inconclusive results, and should be repeated.

We did, however, observe a clear dependence of the measured spot size on the rf frequency. From a minimum value of $\sigma_y \approx 9$ μm at $\Delta f_{rf} = -5$ kHz, the spot size increased to $\sigma_y \approx 13$ μm at $\Delta f_{rf} = +10$ kHz (see ATF logbook no. 13, p. 149). This effect is not understood, and it is oppposite to that expected from a change in the damping partition number.

6 Summary and Outlook

We have analyzed the various effects that may contribute to the equilibrium emittance of the ATF damping ring: linear coupling, spurious dispersion, gas scattering and intrabeam scattering.

In doing so, we have found a few inconsistencies, both between different theories, between theories and simulations, and between theories, simulations and measurements. For example, there are at least three different predictions for the tune dependence of the vertical emittance. The interferometric measurement hardly showed any sensitivity except for a slow increase towards the difference resonance, and an apparent minimum near the sum coupling resonance. Similarily, the vertical spot size was found to be completely insensitive to vertical orbit bumps in the sextupoles and to changes in the skew quadrupole strengths. Instead, it showed an unexpectedly strong dependence on the beam current and the gas pressure. We attribute this to a peculiar feature of the interferometric measurement method, in which beam tails are weighted strongly. Such transverse tails are populated by intrabeam scattering and by gas scattering. We estimate that both these scattering processes contribute in comparable magnitude. The two effects are not easily distinguished as the vacuum pressure changes with the beam current.

The effects of intrabeam scattering calculated according to the le-Duff and the Bjorken-Mtingwa formalism are in rough agreement. Both calculations predict an emittance increase of about 100% for a 5 mA bunch current and a 1% transverse emittance ratio. We found that introducing a cutoff for rare single-scattering events did not change this estimate. Attempts were made to quantify the actual effect of intrabeam scattering, by measuring the current-dependent bunch length, energy spread, beam size, and the beam lifetime near the difference coupling resonance [32]. Bunch lengthening and energy spread increase due to intrabeam scattering of roughly 20% were observed at a bunch current of 1.2 mA. This indicates a vertical-to-horizontal emittance ratio of about 1%, consistent with the interferometric spot size extrapolated to zero pressure. Wire-scanner measurements in the extraction line indicated a slightly larger emittance ratio (2%-3%)[33], but the emittance here is almost certainly degraded by a nonlinear septum field [34]. A 1% emittance ratio is the ATF design goal.

In the future, turn-by-turn orbit data sampled at two BPMs could be used to infer all four linear coupling terms, the optimum locations for coupling correction, and even the higher-order nonlinear optics. The dependence of beam lifetime, bunch length, energy spread, and emittance on the rf voltage should be explored more carefully. Improvements of the transverse dynamic aperture would make the Touschek lifetime a useful diagnostic for emittance tuning. Finally, the effect of the rf frequency on the measured spot size could be further investigated.

7 Acknowledgements

We acknowledge strong support by K. Takata, M. Ross and R. Ruth. We also thank M. Minty, M. Ross and R. Ruth for several useful suggestions. F. Schmidt and R. Bartolini from CERN provided the SUSSIX

program for the normal-form analysis of turn-by-turn orbit data.

References

[1] T. Raubenheimer, "The Vertical Emittance in the ATF Damping Ring", Nucl. Instr. Meth. A 335, p. 1 (1993).

[2] F. Hinode *et al.*, "ATF Design and Study Report", KEK Internal Report 95-4 (1995).

[3] R. Ruth, private communication (1998).

[4] R. Bartolini and F. Schmidt, "Sussix: A Computer Code for Frequency Analysis of Non-Linear Betatron Motion", CERN SL/Note 98-017 (AP) (1998).

[5] M. Minty and T. Naito, private communication (1998).

[6] T. Okugi, H. Hayano, K. Kubo, T. Naito, N. Terunuma, J. Urakawa, F. Zimmermann, "Lifetime Measurement of ATF Damping Ring", presented at the 6th European Particle Accelerator Conference (EPAC 98), Stockholm, Sweden, 22 – 26 June, 1998, SLAC-PUB-7859 and KEK ATF Internal Report ATF 98-15 (1998).

[7] G. Guignard, "Adjustment of Emittance Ratio by Coupling Control in Electron-Positron Storage Rings", Proc. of 11th International Conference on High-Energy Accelerators, Geneva, p. 682 (1980).

[8] G. Guignard, "Betatron Coupling and Related Impact of Radiation", Phys. Rev. E, vol. 51, no. 6, p. 6104 (1995).

[9] F. Willeke and G. Ripken, "Methods of Beam Optics", Cornell Summer School, AIP Proceedings 184, and DESY 88-114 (1988).

[10] P. Bryant, "A Simple Theory for Weak Betatron Coupling", CERN Accelerator School, CERN 89-05 (1989)

[11] M. Minty and M. Woodley, "Summary of Accelerator Physics Studies at KEK/ATF", ATF-98-12 (1998).

[12] F. Zimmermann, M.G. Minty and H. Hayano, "Measurements of Betatron Coupling at the ATF Damping Ring", SLAC/AAS-95 and KEK ATF Internal Report ATF 98–22 (1998).

[13] K. Oide, private communication (1998).

[14] H. Grote and F. C. Iselin, "The MAD Program, Version 8.1, User's Reference Manual", *CERN/SL/* 90-13 (AP) (1990).

[15] A.W. Chao, "Evaluation of Beam Distribution Parameters in an Electron Storage Ring", J. Appl. Phys. 50, p. 595 (1997).

[16] K. Oide, private communication (1998).

[17] K. Ohmi, K. Hirata, K. Oide, "From the Beam-Enevlope Matrix to Synchrotron Radiation Integrals", Phys. Rev. E 49, p. 751 (1994).

[18] The SAD program was written by K. Oide *et al*, unpublished.

[19] K. Kubo, private communication (1998).

[20] P. Emma, J. Irwin, N. Phinney, P. Raimondi, N. Toge, N. Walker, V. Ziemann, "Beam Based Alignment of the SLC Final Focus Sextupoles", Proc. of IEEE PAC 1993, San Francisco, p. 116 (1993)

[21] T.O. Raubenheimer, "Skew Quadrupoles Based on Sextupole Trim Windings for the ATF", ATF-97-22 (1997).

[22] K. Kubo and J. Urakawa, private communication (1998).

[23] R. Bartolini and F. Schmidt, "Normal Form via Tracking or Beam Data", LHC Project Report 132, and Part. Acc. (in press) (1997).

[24] Y. Takayama and S. Kamada, "Spatial Coherence of Bending Magnet Radiations and Application Limit of the Van Citter Zernike Theorem", KEK Preprint 98–116, submitted to Phys. Rev. E (1998).

[25] Y. Takayama and S. Kamada, "Is the SR interferometer available to measure electron beam sie at ATF Damping Ring?", ATF 98–25w (1998).

[26] F. Zimmermann, M.G. Minty, J.L. Turner, M.D. Woodley, J. Urakawa, H. Hayano, K. Kubo, T. Mimashi, N. Terunuma, N. Toge, T. Okugi, "Transverse Acceptance Studies at the ATF Damping Ring", presented at the *XVII International Conference on High Energy Accelerators (HEACC'98)*, Dubna, Russia, September 7–12, *SLAC-PUB-7931* (1998).

[27] "Review of Particle Properties", Particle Data Group, Phys. Lett. B239 (1990).

[28] J. Le Duff, "Single and Multiple Touschek Effects", CERN Accelerator School, West Berlin, Germany, CERN 89-01, p. 573 (1989)

[29] A. Piwinski, Proc. 9th Int. Conf. High Energy Accelerators, p. 405 (1974).

[30] J.D. Bjorken and S. Mtingwa, "Intrabeam Scattering", Part. Acc. 13, p. 115 (1983).

[31] T.O. Raubenheimer, "The Core Emittance with Intrabeam Scattering in e^+/e^- Rings", Part. Acc. (1995).

[32] K. Bane, T. Kotseroglou, T. Naito, T. Okugi, J. Urakawa, F. Zimmermann, "Bunch Lengthening and Current-Dependent Energy Spread at the ATF Damping Ring", ATF report in preparation (1998).

[33] H. Hayano, unpublished (1998).

[34] M. Ross, unpublished (1998).

[35] J. Bengtsson, "Non-Linear Transverse Dynamics for Storage Rings with Applications to the Low-Energy Antiproton Ring (LEAR) at CERN", CERN 88-05 (1988).

[36] J. Laskar, C. Froeschlé and A. Celletti, "The Measure of Chaos by the Numerical Analysis of the Fundamental Frequencies. Application to the Standard Mapping", Physica D 56, p. 253 (1992).

[37] R. Bartolini, A. Bazzani, M. Giovannozzi, W. Scandale, and E. Todesco, "Tune Evaluation in Simulations and Experiments", Part. Acc. 56, p. 167 (1996).

A Measuring the Dynamic Aperture with Orbit Bumps

At low current, the beam lifetime in the ATF damping ring is limited by gas scattering along with a small dynamic aperture [6, 26]. We determined the dynamic aperture by measuring the beam lifetime as a function of collimation amplitude. A similar technique is used at LEP [3]. Since at the ATF dedicated movable collimators are not available, we instead varied the physical aperture by means of local orbit bumps. As bump locations, we selected places with tight beam-pipe dimensions. For the vertical plane, this was the extraction kicker chamber, where the vertical full aperture is only 7 mm. For the horizontal plane we used a bump in the septum region, with a full beam pipe diameter of 14 mm. The result of these measurements is depicted in Fig. 17. The dynamic aperture is the difference between the physical half aperture and half the scan range over which the lifetime is approximately constant. In both planes, it is not much larger than 1 mm, and thus similar to earlier dynamic-aperture estimates based on beam lifetime measurements and on the response to global orbit distortions [26].

The right picture also includes a data point measured on the linear coupling resonance (difference resonance). The estimated acceptance in this case is about 30% higher. Our acceptance estimation assumes that the beam lifetime is only due to gas scattering, which dispells particles outside of the dynamic aerture. The difference between measurements taken on and off the coupling resonance indicates that, at the nominal operating point about 30% of the beam lifetime is not due to gas scattering, but to the Touschek effect. This is a much larger fraction than in early 1998 [26] (at that time about 5%), reflecting both a smaller vertical emittance and an improved vacuum pressure.

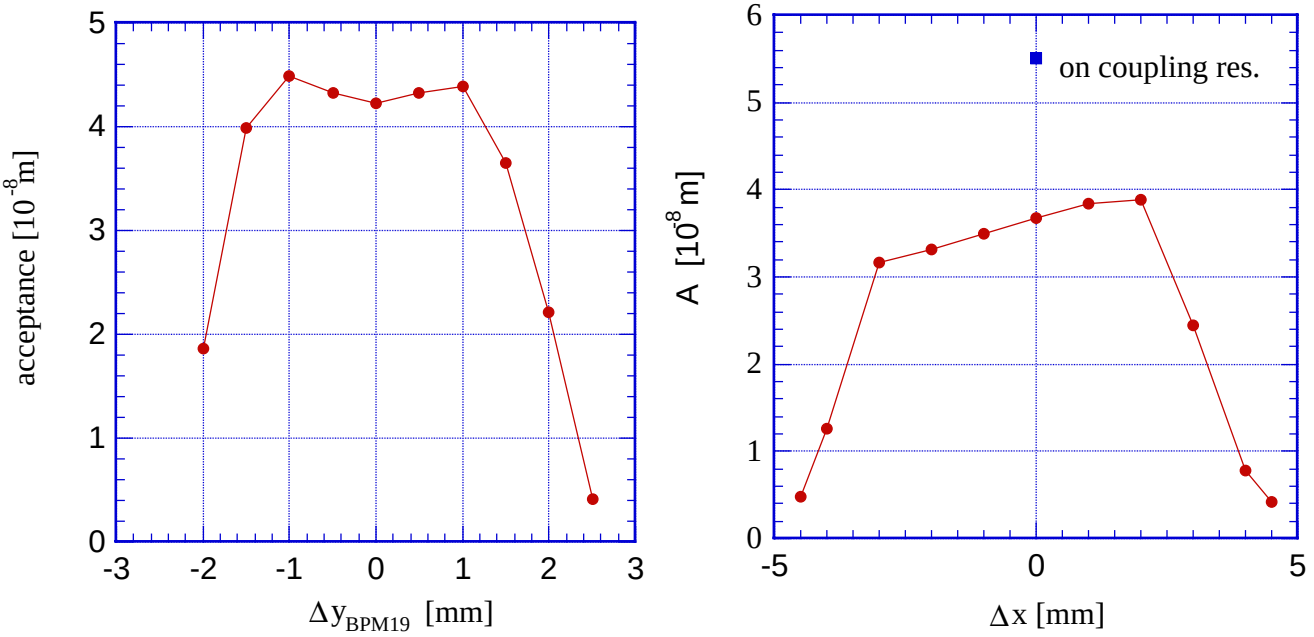

Figure 17: Transverse acceptance, inferred from the beam current decay and the time-dependent pressure, vs. the orbit bump amplitude at an aperture restriction: (left) vertical bump at BPM19, next to the extraction kicker chamber with a full vertical aperture of 7 mm; (right) horizontal bump at the extraction septum with a full aperture of 14 mm. One data point taken on the coupling resonance is also shown, revealing that, at the nominal working point, about 30% of the beam lifetime is due to the Touschek effect.

B Variation of Beta Functions with the Tune

In order to interpret the results from the interferometer, in particular the reponse to tune changes, it is useful to know the variation of the beta functions with the betatron tunes. The results of measurements and simulations are shown in Fig. 18. The figure illustrates that, at the nominal working point, the vertical beta function is fairly insensitive to changes in the QF2R magnet strength.

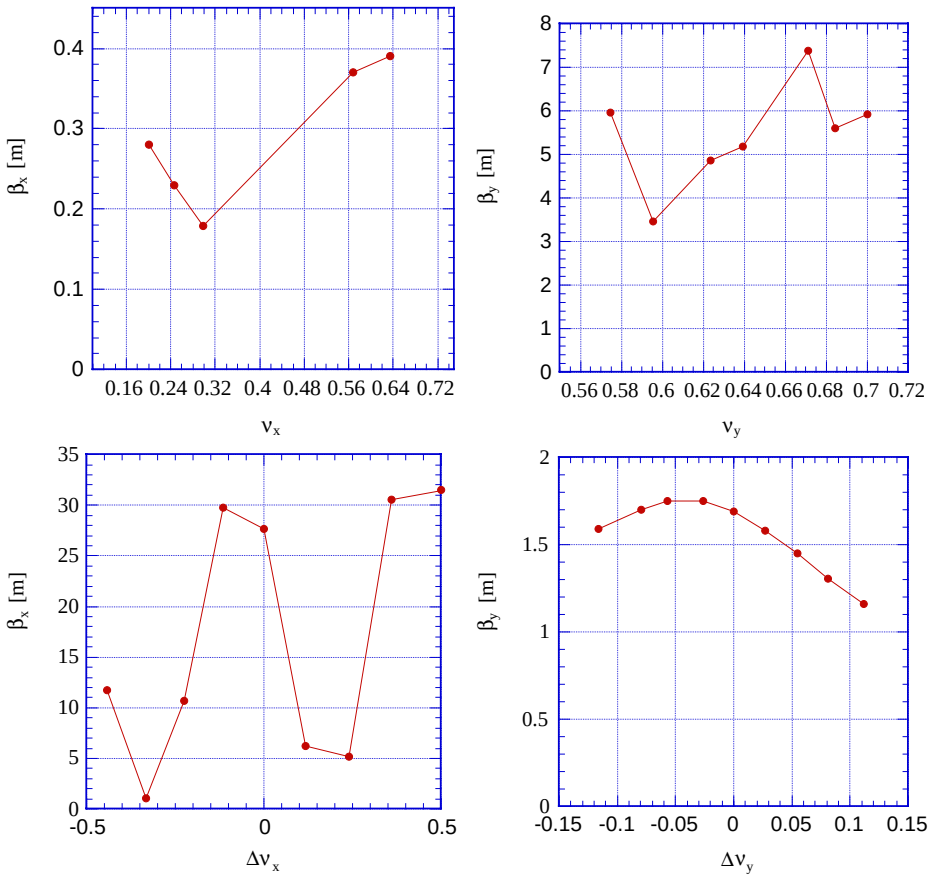

Figure 18: Variation of beta function with the betatron tune, when the strength of the main quadrupole string QF2R is varied: (top) measured horizontal and vertical beta functions at the synchrotron light source vs. the respective tunes; (bottom) simulated variation of the beta functions at some point in the ring as a function of tune change. In the simulation, the QF2R strength was varied over a two times larger range than in the measurement.

C Using SUSSIX to Extract the Linear Coupling Coefficients from Turn-By-Turn Orbit Data

In the future, two high-resolution turn-by-turn beam-position monitors will become available, the information of which can be used to calculate the 4 linear coupling coefficients with the SUSSIX program [4]. The optimum amplitude and phase for an efficient correction is then easily obtained. In the paragraphs below,

we sketch the algorithm and the steps required by the user. Quite similarily the nonlinear Hamiltonian coefficients can be obtained.

Suppose the two BPM are close by, with a 4×4 R matrix describing the linear beam transport from BPM no. 1 to BPM no. 2. The orbit data at these BPMs can be transformed into linearly normalized phase-space coordinates at BPM 1 by two successive transformations:

$$\begin{aligned} x_1' &= (x_2 - R_{11}x_1)/R_{12} \\ y_1' &= (y_2 - R_{33}y_1)/R_{34} \end{aligned} \tag{28}$$

and

$$\begin{aligned} \hat{x} &= x_1/\sqrt{\beta_x} \\ \hat{p}_x &= \frac{\alpha_x}{\sqrt{\beta_x}}x_1 + \sqrt{\beta_x}x_1' \\ \hat{y} &= y_1/\sqrt{\beta_y} \\ \hat{p}_y &= \frac{\alpha_y}{\sqrt{\beta_y}}y_1 + \sqrt{\beta_y}y_1' \end{aligned} \tag{29}$$

These coordinates sampled over many turns are the input to the SUSSIX code. SUSSIX expresses the coordinates in the resonance basis:

$$h_x^+ = \hat{x} + \hat{p}_x = \sqrt{2J_x}e^{-i(\phi_x+\phi_{x0})} \tag{30}$$

$$h_x^- = \hat{x} - \hat{p}_x = \sqrt{2J_x}e^{i(\phi_x+\phi_{x0})} \tag{31}$$

$$h_y^+ = \hat{y} + \hat{p}_y = \sqrt{2J_y}e^{-i(\phi_y+\phi_{y0})} \tag{32}$$

$$h_y^- = \hat{y} - \hat{p}_y = \sqrt{2J_y}e^{i(\phi_y+\phi_{y0})} \tag{33}$$

where $J_{x,y}$ are the action variables, and $\phi_{x,y}$ the betatron phases. The normal form coordinates $\zeta_{x,y}^{\pm}$ are related to the coordinates $h_{x,y}^{\pm}$ by a generating function F_r: $\zeta = e^{-:F_r:}h$. In the normal form coordinate frame, the linear coupling is most generally characterized by 4 complex coefficients f_{jklm}::

$$F_r = f_{1010}\zeta_x^+\zeta_y^+ + f_{1001}\zeta_x^+\zeta_y^- + f_{0110}\zeta_x^-\zeta_y^+ + f_{0101}\zeta_x^-\zeta_y^- \tag{34}$$

To first order in the linear coupling strength, the linearly normalized coordinates h then evolve according to the generating function F_r. For example, the coordinate h_y^- at turn number N is given by:

$$\begin{aligned} h_y^-(N) = &\sqrt{2I_y}e^{i(2\pi\nu_y N+\psi_{y0})} + \\ &-2i\sum_{jklm} l f_{jklm}(2I_y)^{\frac{j+k}{2}}(2I_y)^{\frac{l+m-1}{2}}e^{i[(k-j)(2\pi n u_x N+\psi_{x0})+(1+m-l)(2\pi\nu_y N+\psi_{y0})]} \end{aligned} \tag{35}$$

The different terms in this sum correspond to different lines in the Fourier spectrum of h_y^- [35]. Recently, very precise techniques have been developed to calculate the amplitude and phase of such spectral lines [36, 37]. These are incorporated in the SUSSIX code. Once the generating coefficients f_{jklm} are obtained, the coefficient in the equivalent Hamiltonian follow from the relation

$$f_{jklm} = \frac{h_{jklm}}{1 - e^{-i[2\pi\{(j-k)\nu_x+(l-m)\nu_y\}]}} \tag{36}$$

For example, consider the spectrum of h_y^-. A line at ν_y corresponds to the vertical base tune. Other lines arise due to the linear coupling. A line at $-\nu_x$ corresponds to f_{1010}, and a line at ν_x to f_{0110}. The other terms are obtained from the spectrum of h_y^+, where a line at ν_x is related to f_{0101}, and at ν_x to f_{1001}. Defining $\hat{\phi} = \pi((j-k)\nu_x + (l-m)\nu_y)$, for the first two terms we can express the amplitude and phase of the Hamiltonian coefficient h_{jklm} as

$$|h_{jklm}| = \left| \frac{A_{h_y^-,-1,0} \sin\hat{\phi}}{A_{h_y^-,0,1}} \right| \tag{37}$$

$$\phi_{jklm} = \phi_{h_y,-1,0} + (j-k)\phi_{h_x^-,1,0} + (l-m-1) * \phi_{h_y^-,0,1} + \pi/2 + \mathrm{sign}(\hat{\phi})\pi/2 + \hat{\phi} \tag{38}$$

where, *e.g.*, $A_{h_y^-,-1,0}$ is the amplitude of the $-\nu_x$ line in the spectrum of h_y^-, and $\phi_{h_y^-,-1,0}$ is its phase. A similar expression holds for the other two cases, where simply all indices j and k, as well as l and m must be interchanged.

We tested this procedure for an example map, consisting of two linear rotations with phase advances ($\nu_{x1} = 0.3$, $\nu_{y1} = 0.21$) and ($\nu_{x2} = 0.58$m $\nu_{y2} = 0.22$) respectively, 2 observation points, and a skew quadrupole at BPM 1 of integrated strength $k_s = 0.03$ m^{-1}. Figure 19 shows an example of simulated raw data for one BPM, and Fig. 20 the linear phase space coordinates $\hat{x}, \hat{p}_x, \hat{y}, \hat{p}_y$, reconstructed according to Eqs. (28) and (29).

From these data, the SUSSIX program calculates the amplitude and phases of different lines in the FFT spectra of $\zeta_{x,y}^{\pm}$. In our example, the horizontal tune line in the ζ_x^- frequency spectrum has an amplitude of 1.02 mm$^{-1/2}$ and a phase $-108°$. The amplitude of the vertical tune line in the ζ_y^- spectrum is similar, 1.03 mm$^{1/2}$, and its phase is $-73°$. For the $+\nu_x$ line in the vertical ζ_y^- spectrum the amplitude is 0.0093 mm$^{1/2}$ and the phase 135°; finally, the amplitude of the $-\nu_x$ line is 0.0077 mm$^{1/2}$ with a phase of 70°. From these 8 numbers, using Eqs. (37) and (38), we can deduce the Hamiltonian coefficients: $|h_{1010}| = 0.0075$, $\phi_{1010} \approx 0$ (-5×10^{-6}°), $|h_{1001}| = 0.00746$ and $\phi_{1001} \approx 0$ (-4×10^{-6}°). The amplitudes are equal to the expected value $K_s/4$ and the phase is zero, since we have placed the skew quadrupole at the same location as our reference BPM. The coefficients h_{0101} and h_{0110} need not be calculated, as they are related to the other two via $h_{1010} = h_{0101}$ and $h_{1001} = \overline{h_{0110}}$.

We conclude that from simulated BPM data we can correctly reconstruct the amplitude and phase of all 4 complex coupling coefficients with an accuracy much better than 1% in amplitude, and as good as 10^{-5} rad in phase. This should be more than adequate for practical applications of this method.

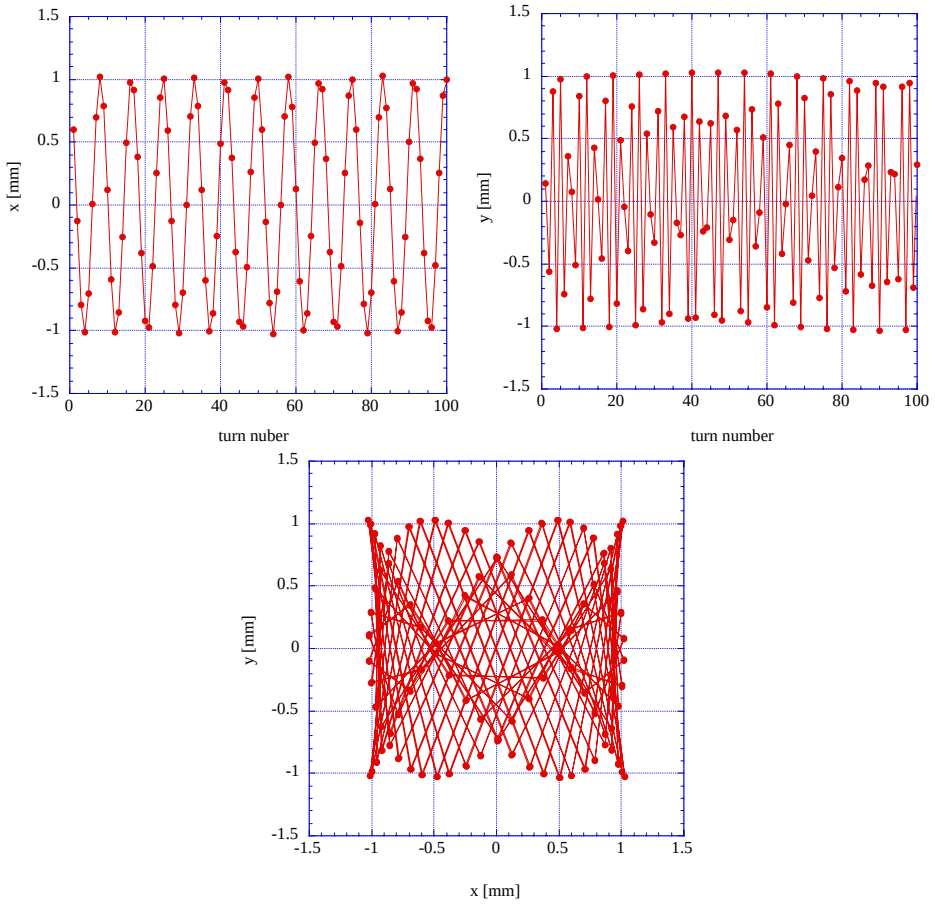

Figure 19: Simulated horizontal and vertical BPM raw data.

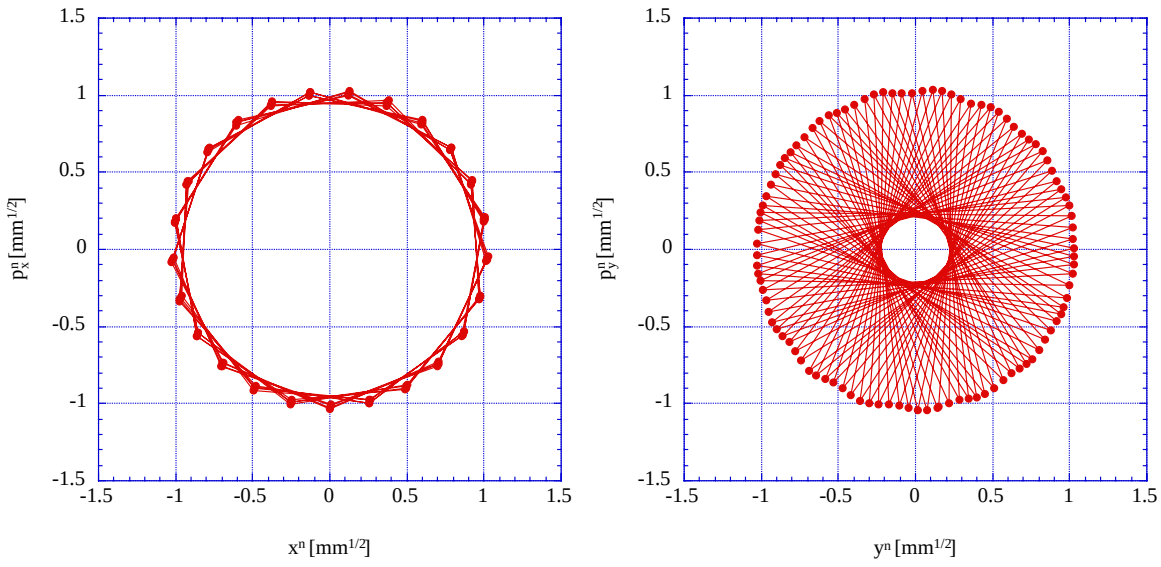

Figure 20: Simulated horizontal and vertical turn-by-turn phase space coordinates, reconstructed from the raw data according to Eqs. (28) and (29).